Generation of Superponderomotive Electrons in Multipicosecond Interactions of Kilojoule Laser Beams with Solid-Density Plasmas

A. Sorokovikova, A. V. Arefiev, C. McGuffey, B. Qiao, A. P. L. Robinson, M. S. Wei, H. S. McLean, and F. N. Beg

Phys. Rev. Lett. **116**, 155001 — Published 12 April 2016
DOI: 10.1103/PhysRevLett.116.155001

Generation of superponderomotive electrons in multi-picosecond interactions of kilo-Joule laser beams with solid-density plasmas

A. Sorokovikova,[1] A. V. Arefiev,[2] C. McGuffey,[1,*] B. Qiao,[1] A. P. L. Robinson,[3] M. S. Wei,[4] H. S. McLean,[5] and F. N. Beg[1,+]

[1] *Center for Energy Research, University of California, San Diego, California 92093, USA*

[2] *Institute for Fusion Studies, The University of Texas, Austin, Texas, 78712, USA*

[3] *Central Laser Facility, STFC Rutherford-Appleton Laboratory, Didcot, OX11 0QX, UK*

[4] *General Atomics, San Diego, California, 92186, USA*

[5] *Lawrence Livermore National Laboratory, Livermore, California, 94511, USA*

(Resubmission date: March 16, 2016)

Interaction of a multi-picosecond (ps), kilo-Joule laser pulse with a surface of a solid target has been shown to produce electrons with energies far beyond the free-electron ponderomotive limit, $m_ec^2a_0^2/2$. Particle-in-cell simulations indicate that increase in the pulse duration from 1 to 10 ps leads to formation of a low-density shelf (about 10% of the critical density). The shelf extends over 100 μm toward the vacuum side, with a non-stationary potential barrier forming in that area. Electrons reflected from the barrier gain super-ponderomotive energy from the potential. Some electrons experience even greater energy gain due to ponderomotive acceleration when their "dephasing rate", $R = \gamma - p_x/m_ec$, drops well below unity, thus increasing acceleration by a factor $1/R$. Both 1D and 2D simulations indicate that these mechanisms are responsible for generation of extensive thermal distributions with $T_e > 10$ MeV and a high-energy cutoff of hundreds of MeVs.

Laser-plasma interaction (LPI) at relativistic intensities (> 10^{18}W/cm^2) offers an efficient source of fast electrons with energy above 10's of MeV, which is of fundamental interest for a range of applications including accelerator science [1], laboratory astrophysics, and inertial fusion energy [2]. Relativistic LPIs in low-density plasmas have a notable ability to produce high-energy electrons through several known mechanisms such as wake-field [3-5] and direct laser accelerations [6].

However, solid target interaction with such a laser is complex, spanning several orders of magnitude difference in the characteristic temporal and spatial scales between solids and low-density preplasma [7-9]. On sub-picosecond timescales, if the preplasma scale length is steep (or zero), fast electrons are produced predominantly by relativistic **j** × **B** heating [10], resulting in a Boltzmann-like energy distribution [11-13] with a slope temperature close to the ponderomotive scaling $T_p = [(1 + a_0^2)^{1/2} - 1]m_ec^2$ [14] and maximum energy near the free electron ponderomotive limit $E_p = m_ec^2a_0^2/2$ ($a_0 = eE_0/m_ec\omega$ is the laser field amplitude). When a large-scale preplasma [15-17] is created by intrinsic laser prepulses, electrons of energy > E_p can be produced due to stochastic acceleration [18, 19]. However, so far, most studies have focused only on subpicosecond laser cases.

High-intensity petawatt laser facilities that deliver multi-picosecond (ps) kilojoule (kJ) laser pulses have become available, such as OMEGA-EP [20], LFEX [21], PHELIX [22], PETAL [23], and NIF-ARC will become available soon [24]. In this new multi-ps kJ regime, the nature of preplasma heavily evolves with time, instabilities and self-generated electromagnetic fields grow significantly, thus the dynamics of LPI and the characteristics of fast electron generation are inherently different from those in the sub-ps regime. Considerable preplasma is expected to build up even for a high contrast laser due to the thermal expansion of electrons, and on multi-ps timescales the ions also move collectively. Recent particle-in-cell (PIC) simulations [25] demonstrated ~ 5ps evolution of solid target interaction with lasers, but their scope is limited to a steep preplasma density gradient and a low-Z deuterium plasma. The underlying physics of multi-ps, kJ LPI are unexplored.

In this Letter, we report theoretical and numerical studies on plasma dynamics and fast electron generation inherent to multi-ps LPIs, yet previously unexplored. Our one- and two-dimensional (1D, 2D) PIC simulations reveal that electrons with energy far exceeding the free electron ponderomotive limit are produced, and temperature and maximum energy of these superhigh energy electrons significantly increase as laser pulse duration increases from 1 to 10ps. We find that on multi-ps timescales the electron density distribution self-evolves into a step-like profile jumping from critical density n_c to γ_0n_c [$n_c = \omega^2m_e/4\pi e^2$ and $\gamma_0 = (1+ a_0^2)^{1/2}$] followed with a long, flat shelf extending to the subcritical region. A deep, broad electrostatic potential profile is induced in the shelf. We prove that the presence of this shelf and the co-located potential are responsible for the energetic electrons. Particle tracing in the simulation and an analytical model have explained that the evolving potential itself imparts significant energy to some electrons and that further acceleration results from the potential's reduction of electrons' dephasing rate $R = \gamma - p_x/m_ec < 1$ [26, 27]. Since the duration and volume in which the antidephasing occurs increase with pulse duration, the number and energy of super-ponderomotive electrons increase. We show that the antidephasing acceleration occurs even when multi-dimensional effects are included.

1D simulations have been carried out using the PIC code, EPOCH [28]. We choose a simulation domain spanning [-600, 200] μm in x with 64000 cells. The corresponding time-step allows us to correctly resolve the dynamics of the accelerated electrons [29]. All four sides of the domain have an open boundary condition which allow particles and fields to leave the domain freely. 1000 electrons and 100 Al^{13+} ions per cell are loaded for a solid (2.7g/cm^3) aluminum target, which represent different numbers of real particles. The initial electron density is $n_e(x) = Zn_{solid}/\{1 + \exp[-(x - x_0)/L]\}$, shown in Fig. 1(a), where $L = 10$μm, $Z = 13$ and $x_0 = 150$μm. The preplasma extends to $x = 0$, reaching 2.4 x 10^{17}cm^{-3}. The space $x < 0$ is vacuum, allowing room for thermal expansion of plasma electrons throughout multi-ps. Initial electron and ion temperatures are both chosen to be 100eV. A 1μm wavelength laser with peak intensity 10^{20}W/cm^2 ($a_0 = 8.54$) is injected at $x = -600$μm, and reaches the plasma at $x = 0$ at $t \equiv t_0$ which is 2.0ps for all 1D simulations here. The laser field E_z has temporal profile $\sin^2(\pi t/\tau)$, where τ is the laser pulse duration.

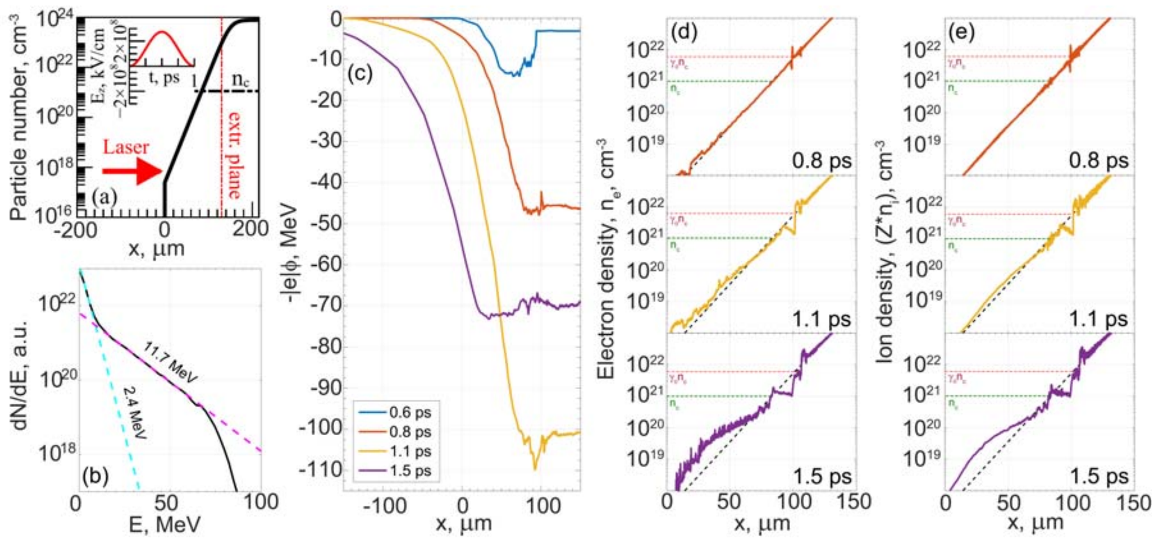

FIG. 1. (color online) 1D PIC simulation of a 1ps laser interaction with a solid Al target:(a) initial electron density profile; (b) energy spectrum collected at the extraction plane; (c) the electrostatic potentials at various times t-t_0 = 0.6, 0.8, 1.1, and 1.5 ps.; (d) and (e) the corresponding electron and ion density profiles at times as indicated.

The extraction plane diagnostic, which collects the information of passing particles, is located at x=130μm.

The spectrum (Fig. 1(b)) clearly indicates two slope temperature components: the ponderomotive one with 2.4MeV and the superhigh energy one with 11.7MeV, with maximum energy 90MeV, far exceeding the free electron ponderomotive limit ~ 25MeV.

Figures 1(c)-1(e) plot, respectively, the self-generated electrostatic potentials, electron and ion densities at times t-t_0 = 0.6, 0.8, 1.1, and 1.5ps (laser pulse duration is τ = 1ps). The potential is calculated from zero at the left boundary and integrating over the electric field. For this pulse duration, new behaviors characteristic to multi-ps kJ LPIs are onset. First, the strong laser ponderomotive pressure (30GBar at 10^{20}W/cm^2) keeps compressing preplasma electrons at the critical density n_c, which eventually forms a steep critical surface jumping from n_c to $\gamma_0 n_c$. The laser front is depleted here within a skin depth, passing energy to electrons through $\mathbf{j} \times \mathbf{B}$ heating, where the final energy spectrum of these electrons obeys the ponderomotive scaling [14]. Secondly, a flat shelf electron density profile is self-formed within the near-critical region ($0.1n_c < n_e < n_c$) [see 1(d)]. Note that the ions also move in the 1ps timescale [see Fig. 1(e)]. Thirdly, corresponding to this step-function-like density profile, a deep, broad electrostatic potential profile [1(c)] is induced, which evolves with time, and electrons in the near-critical region oscillate inside the potential.

To analyze the mechanism of the above superhigh energy electron production, we consider a 1D model for single electron motion in the presence of laser fields **E** and **B** and an electrostatic potential φ as $d\mathbf{p}/dt = -e(\mathbf{E}+\mathbf{v}\times\mathbf{B}/c)+e\nabla\phi$ and $d\gamma/dt = -\mathbf{v}\cdot\mathbf{E}+\mathbf{v}\cdot\nabla\varphi$, where $\mathbf{p} = \gamma m_e \mathbf{v}$ and $\gamma = (1 + p^2/m_e^2c^2)^{1/2}$ are electron momentum and relativistic factor respectively. We assume the laser is a planar wave with the vector potential $A\mathrm{e}_z = a_0 \cos(\omega t - k_x x)\mathrm{e}_z$. After differentiating, we can obtain an electron's motion in the transverse and longitudinal directions respectively as $dp_z/d\tau_c = d(eA)/d\tau_c$ and $d(\gamma - p_x/m_ec)/d\tau_c = -(e/m_ec)\partial\phi/\partial x$, where $\tau_c = t - x/c$. If assuming that the electron is initially at rest, we get a key integral of electron transverse motion as $p_z = eA$. Further, if $\varphi = 0$, another integral of electron longitudinal motion can be found, $R = \gamma - p_x/m_ec = 1$. In the low density regions where most acceleration takes place, the laser phase velocity is nearly c, and R represents the electron's dephasing rate [30]. The maximum energy electrons can gain in this case is $E_p = m_ec^2a_0^2/2$.

However, during a multi-ps LPI, a deep, broad electrostatic potential profile is induced [Fig. 1(c)], which leads to $R \neq 1$. Therefore, we can write an electron's equation of longitudinal motion as

$$\frac{dp_x}{dt} = \frac{1}{R}\frac{e^2A}{m_ec}\frac{dA}{dt} + e\frac{\partial\phi}{\partial x}, \quad (1)$$

$$R = 1 - \frac{e}{m_ec}\int\frac{\partial\phi}{\partial x}d\tau_c = 1 - \frac{e}{m_ec}\int\frac{\partial\phi}{\partial x}\left(1-\frac{v_x}{c}\right)dt. \quad (2)$$

Eqs. (1) and (2) together describe the dynamics of super-high energy electron production in the near-critical shelf region during multi-ps LPI, where a deep electrostatic potential profile develops. The effect of the induced electrostatic potential barrier is not only directly awarding additional energy $e(\delta\phi)$ to electrons, but also linked with the laser ponderomotive acceleration through the dephasing rate R. When electrons oscillate inside the potential profile, they experience antidephasing ($\partial\phi/\partial x>0$, $R<1$) in its left half and dephasing ($\partial\phi/\partial x<0$, $R>1$) in its right half. That respectively results in acceleration or deceleration under the laser ponderomotive force by a factor of $1/R$.

As seen in Fig. 1(c), because the plasma expansion dominates on the vacuum side, the left half of the potential barrier is much wider and deeper than the right. So electrons always experience longer and larger antidephasing than dephasing. From the viewpoint of a non-stationary Hamiltonian theory [31-34], antidephasing (resulting in a high-energy electron acceleration) may be interpreted as a reduction of the "moving-frame" Hamiltonian, $H(\tau_c, x) = m_ec^2\gamma_e - cp_x - e\phi$, where $\gamma_e = (1 + p^2/m_e^2c^2 + a_0^2/2)^{1/2}$.

Note that the profile of the potential evolves during the multi-ps LPI. A broader, deeper left wall and a sharper right wall potential should produce more superhigh energy electrons, because it creates a large volume for antidephasing. Note that the left-most side of the potential barrier in Fig. 1 can directly accelerate electrons.

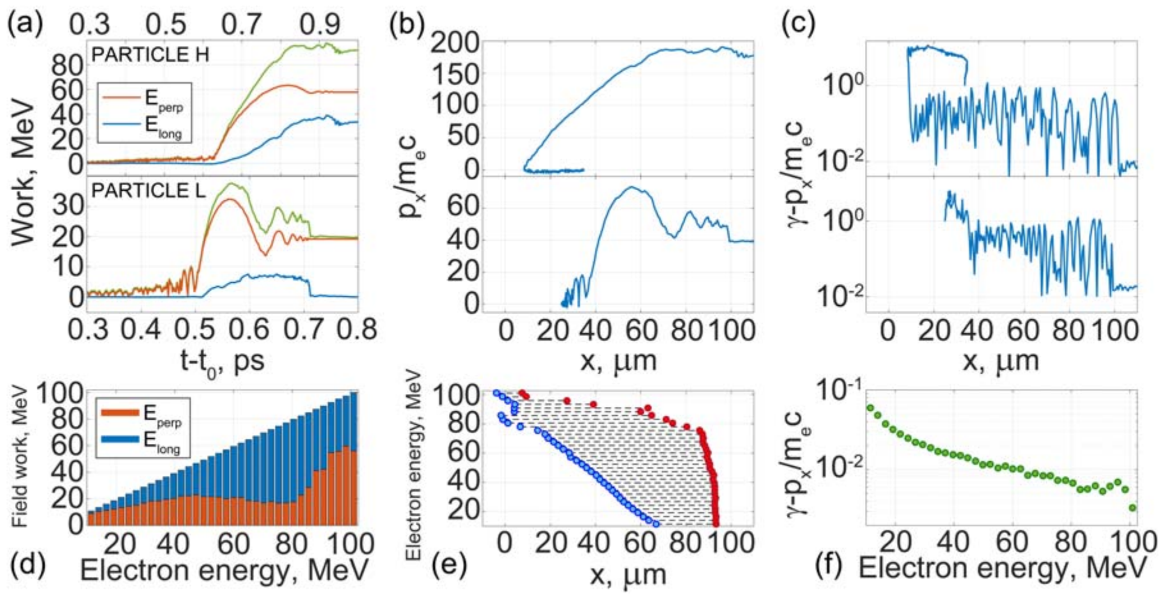

FIG. 2. (color online) (a) The work done on two characteristic test particles by longitudinal electric fields such as the electrostatic potential (blue), by transverse fields (brown) and total (green); (b)-(c) The momentum $p_x(t)$ and dephasing rate R(t) and for the same electrons; (d)The average work done by each field component on tracked electrons binned by their final energy; (e) energy bins of tracked electrons versus their average original positions (red) and farthest extent to the left (blue); (f) the average final dephasing rate R of fast electrons binned by their final energies.

Figure 2 displays information from recorded trajectories of individual particles. Fig. 2(a) shows the time histories of work done by electric field components on two particles exemplifying superhigh acceleration ('H', top) and **j** × **B** heating ('L', bottom). Their dephasing rate and momentum time histories are shown in Figs. 2(b) and 2(c), respectively. Both electrons experienced large antidephasing (*R* decreases to << 1) from the left of the potential barrier, which began forming by t - $t_0 \approx 0.6$ ps [Fig. 1(c)]. However, particle H first moved toward the vacuum side then experienced rapid acceleration and antidephasing throughout its transit from x=10μm until it reached maximum energy at x=70μm. As a result, it achieved final p_x/m_ec of 180, 4.5 times greater than particle L and 3.5 times the free-electron ponderomotive limit. Particle L was accelerated with minimal work done by the electrostatic potential, and antidephasing coincided with acceleration only briefly between x=35-55μm, resulting in much lower final p_x/m_ec of 40.

Fig. 2(d) displays the work done by the different field components averaged over all test particles binned by their final energy. The lowest energy particles gain energy predominantly by the perpendicular (laser) field, and intermediate energies (10<E<80 MeV) gain nearly the same quantity (10-20 MeV) from the laser field. The highest energy electrons (>80 MeV) gain significant energy from the longitudinal field (electrostatic potential) and notably experience work greatly exceeding the free-electron ponderomotive limit by the laser field. Fig. 2(e) plots the average original positions and left-most extents of eventual fast electrons. The electrons reaching low and modest energies originate from the steep critical surface, and energy correlates with long travel into the shelf region. The superhighenergy ones (E>80MeV) come from shelf region far from the critical surface. From Fig. 2(f) - the final dephasing rate *R* of fast electrons versus their energy- we can also see that superhigh energy electrons do come from the antidephasing mechanism with final $R \ll 1$.

The evolution of the electrostatic potential profile plays a key role in the antidephasing mechanism. Therefore, electron acceleration in multi-ps LPIs heavily depends on the laser pulse durations τ. Figures 3(a)-3(d) plot electron density profiles late in the interactions for τ = 1, 3, 5 and 10ps respectively. The longer pulse durations significantly enhance both the density steepening and the extension of the long shelf profile. Correspondingly, a much wider and deeper potential barrier is self-formed for longer τ [Fig. 3(f)], leading to longer and greater antidephasing electron acceleration. The temperature and maximum energy of electrons are increased by extension of the laser pulse, see Fig. 3(e). On the other hand, the low-energy spectrum shapes are similar, due to the fixed intensity.

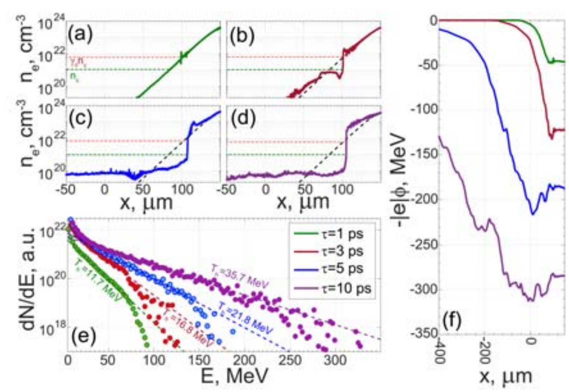

FIG. 3. (color online) (a)-(d) electron density profiles at t-t_0= (0.8, 1.8, 4.2, 6.7) ps for laser durations τ = (1, 3, 5, 10) ps respectively. (e) time-integrated energy spectra of fast electrons entering the solid; (f) corresponding electrostatic potential profiles at the same times as (a)-(d).

To check if the antidephasing mechanism is extant in a multi-dimensional case, 2D simulations were conducted in a system domain spanning x = [-170, 130]μm in the longitudinal direction (18000 cells) resulting in t_0 = 567fs and y = [-30,30]μm in the transverse direction (1200 cells). The density profiles were the same as the 1D simulations with 20 electrons and 5 ions per cell. The laser had transverse Gaussian profile with 10.6μm FWHM and durations τ = 1 and 5ps. Figures 4(a) and 4(b) plot electron density distributions and their longitudinal profiles [4(c)] for both durations. The intense laser propagates deeply into the plasma, reaching the relativistic critical density of 10^{22}cm^{-3}, and a quasistatic lower-density (10^{20} — 10^{21}cm^{-3}) channel is created near the x-axis. Inside the channel, the radial charge separation electric field balances the radial expelling ponderomotive force, allowing fast electrons to be accelerated longitudinally via dynamics similar to the 1D cases. Both the critical density steepening and the self-formation of the near-critical shelf can still be observed inside the channel [4(c)], inducing a broad electrostatic potential profile [4(d)]. The previously discussed acceleration mechanisms still occur in 2D geometry.

Figure 4(e) shows the time-integrated electron energy spectra in 2D simulations. The results are consistent with the 1D results: a large number of super-high energy electrons are produced and their temperature and maximum energy increase for longer pulse duration. The difference between 1D and 2D results at the highest energies can be attributed to weaker potential barrier [compare Fig. 4(d) to 3(f)] due to an additional degree of freedom allowed for plasma expansion, and the strong potential is restricted to the axis, affecting fewer particles.

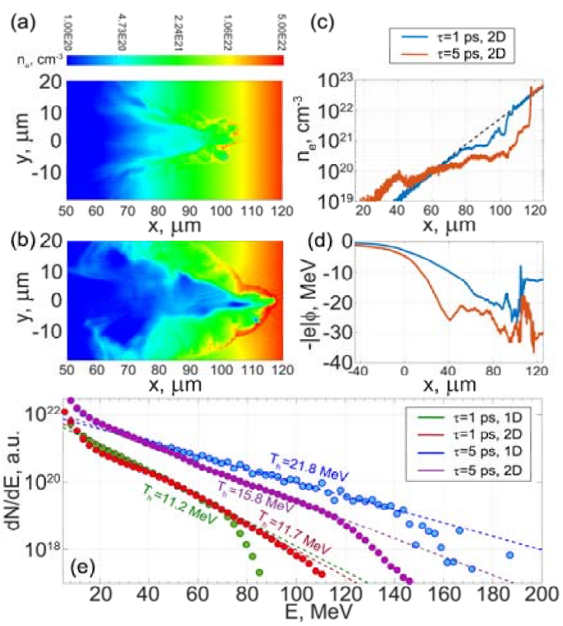

FIG. 4. (color online) 2D PIC simulation results: electron density in 1 ps (a) and 5 ps (b) cases at t-t$_0$ = 0.95 and 3.05 ps, respectively; (c) axial electron density profiles inside the channel of (a) and (b); (d) corresponding electrostatic potential profiles inside the channel; (e) time-integrated electron energy spectra, in comparison with the previous 1D results.

There are other enhanced acceleration mechanisms [35] that might also be at work in multi-dimensional cases. In principle, there are three factors leading to antidephasing: (a) the electrostatic potential barrier discussed here, (b) the electrostatic field in the plasma channel [26, 27], and (c) the reflected electromagnetic wave.

In summary, we have studied intense LPI and fast electron generation in the multi-ps kJ scale regime. It is found that a substantial number of superponderomotive electrons are produced and their temperature and maximum energy significantly increase with the laser pulse duration (1-10ps). The electrostatic potential barrier, which builds up on the subcritical side throughout the multi-ps interaction, increases electron energy through electrostatic acceleration and enhances the ponderomotive acceleration via the anti-dephasing mechanism. Both effects contribute to generation of numerous super-ponderomotive electrons with temperature >10 MeV, and energy cutoff of hundreds of MeVs.

This work was performed under the auspices of U.S. DOE under contracts DE-NA0000870, DE-FG02-05ER54834, and DE-FC02-04ER54789. Simulations were performed using EPOCH code (developed under UK EPSRC Grants No. EP/G054940/1, No. EP/G055165/1, and No. EP/G056803/1) using HPC resources provided by the TACC at the University of Texas. AA was supported by the U.S. DoE through agreements No. DE-NA0002008 and DE-FG02- 04ER54742.

* Corresponding author: cmcguffey@ucsd.edu
+ fbeg@ucsd.edu

[1] T. Tajima and J. M Dawson, Phys. Rev. Lett. **43**, 267 (1979).
[2] J. D. Lindl, Phys. Plasmas **2**, 3933 (1995).
[3] G. A. Mourou, T. Tajima, and S. V. Bulanov, Rev. Mod. Phys. **78**, 309 (2006).
[4] E. Esarey, C.B. Schroeder, and W. P. Leemans, Rev. Mod. Phys. **81**, 1229 (2009).
[5] V. Malka, Phys. Plasmas **19**, 055501 (2012).
[6] A. Pukhov, Z. M. Sheng and J. Meyer-ter-Vehn, Physics of Plasmas **6**, 2847 (1999).
[7] W. Theobald, *et al.,* Phys. Plasmas **13**, 043102 (2006).
[8] T. Ma, *et al.,* Phys. Rev. Lett **108**, 115004 (2012).
[9] A. G. MacPhee *et al.,* Phys. Rev. Lett. **104**, 055002 (2010).
[10] W. L. Kruer and K. Estabrook, Physics of Fluids **28**, 430 (1985).
[11] M. Sherlock, Phys. Plasmas **16**, 103101 (2009)
[12] T. Kluge, T. Cowan, A. Debus, U. Schramm, K. Zeil, and M. Bussmann, Phys. Rev. Lett **107**, 205003 (2011).
[13] J. May, J. Tonge, F. Fiuza, R. A. Fonseca, L. O. Silva, C. Ren, and W. B. Mori, Phys. Rev. E **84**, 025401 (2011).
[14] S. C. Wilks, W. L. Kruer, M. Tabak and A. B. Langdon, Phys. Rev. Lett **69**, 1383 (1992).
[15] A. J. Kemp, Y. Sentoku, and M. Tabak, Phys. Rev. E **79**, 066406 (2009).
[16] B. S. Paradkar, M. S. Wei, T. Yabuuchi, R. B. Stephens, M. G. Haines, S. I. Krasheninnikov, and F. N. Beg, Phys. Rev. E **83**, 046401 (2011).
[17] Y. Ping et *al.,* Phys. Rev. Lett. **109**, 145006 (2012).
[18] B. S. Paradkar, S. I. Krasheninnikov and F. N. Beg, Phys. Plasmas **19**, 060703 (2012).
[19] Z. M. Sheng, K. Mima, Y. Sentoku, M. S. Jovanović, T. Taguchi, J. Zhang, and J. Meyer-ter-Vehn, Phys. Rev. Lett. **88**, 055004 (2002).
[20] D. N. Maywar *et al.,* J. Phys.: Conf. Ser. **112**, 032007 (2008).
[21] N. Miyanaga *et al.,* J. Phys. IV, **133**, 81-87 (2006).
[22] V. Bagnoud *et al*., Appl. Phys. B **100**, 137 (2010).
[23] N. Blanchot *et al*., EPJ. Web of Conferences **59**, 07001 (2013).
[24] C. P. J. Barty *et al.,* Nucl.. Fusion **44**, S266 (2004).
[25] A. J. Kemp and L. Divol, Phys. Rev. Lett. **109**, 195005

(2012).
[26] A. V. Arefiev, B. N. Breizman, M. Schollmeier, and V. N. Khudik Phys. Rev. Lett. **108**, 145004 (2012).
[27] A. P. L. Robinson, A. V. Arefiev, and D. Neely, Phys. Rev. Lett. **111**, 065002 (2013).
[28] T. D. Aeber, K. Bennett, C. S. Brady, A. Lawrence-Douglas, M. G. Ramsay, N. J. Sircombe, P. Gillies, R. G. Evans, H. Schmitz, A. R. Bell and C. P. Ridgers, Plasma Physics and Controlled Fusion **57,** 1-26 (2015).
[29] A. V. Arefiev, G. E. Cochran, D. W. Schumacher, A. P. L. Robinson, and G. Chen, Phys. Plasmas **22**, 013103 (2015).
[30] A. P. L. Robinson, A. V. Arefiev and V. N. Khudik, Phys. Plasmas **22**, 083114 (2015).
[31] P. Mora, Phys. Fluids B **4**, 1630 (1992).
[32] S. A. Yi, V Khudik, S Y Kalmykov and G Shvets, Plasma Phys. Control. Fusion **53**, 014012 (2011).
[33] S. Y. Kalmykov, B. A. Shadwick, A. Beck, E. Lefebvre, S. A. Yi, V. Khudik, and M. C. Downer, AIP Conf. Proc. **1299**, 174 (2010).
[34] S. Y. Kalmykov, A. Beck, S. A. Yi, V. N. Khudik, M. C. Downer, E. Lefebvre, B. A. Shadwick, and D. P. Umstadter, Phys. Plasmas **18**, 056704 (2011).
[35] A. V. Arefiev, V. N. Khudik, and M. Schollmeier, Phys. Plasmas **21**, 033104 (2014).